PROPAGATION OF REALISTIC BEAMS IN UNDERDENSE PLASMA

D. E. Hinkel *L. V. Powers*
R. L. Berger *C. H. Still*
A. B. Langdon *E. A. Williams*

Introduction

The study of parametric instabilities[1] has long been a topic of interest in laser–plasma interactions. Reliable prediction of experimental results requires detailed knowledge of the plasma characteristics (density, temperature and flow profiles) as well as the laser beam structure (phase and intensity modulation information). Hydrocodes such as LASNEX[2] and experimental measurements yield data about the plasma, and experimental measurements[3–5] and laser-beam propagation codes[6] provide relevant information about beam characteristics.

In this article, we examine two physical mechanisms that demonstrate the effect of beam structure on its propagation through underdense plasma. First, we discuss the effect of transverse plasma flow on beam deflection. When there is plasma flowing across a beam, the density depressions created by the ponderomotive pressure of the light wave are swept downstream in the flow direction, and the light, which is refracted into the density depression, moves downstream as well.

We present a simple analysis of this problem, which shows that the beam deflection rate scales with the figure of merit $Q \equiv (v_0/v_e)^2 (n/n_c)(1 - n/n_c)^{-1}$, where v_0 (v_e) is the electron quiver (thermal) velocity, n is the electron plasma density, and n_c is the critical plasma density at which light reflects ($n/n_c = \omega_{pe}^2/\omega_0^2$, where ω_{pe} is the electron-plasma frequency and ω_0 is the light-wave frequency). In previous work by Ghosal and Rose,[7] three different expressions for the beam deflection rate were derived—for the subsonic, near-sonic, and supersonic regimes of the transverse flow, respectively. We have derived a more general expression, valid for all transverse Mach numbers M as well as noncircular Gaussian beams, which reduces to the results of Ghosal and Rose[7] in the three Mach number regimes with circular beam cross sections. In the limits of subsonic $M < 1$, near-sonic $M \approx 1$, and supersonic $M > 1$ transverse flow, our expression for the beam deflection rate scales as $\bar{\nu} M/(1 - M^2)^{3/2}$, $1/\bar{\nu}^{1/2}$, and $1/[M(M^2 - 1)^{1/2}]$, respectively, where $\bar{\nu}$ is the ion damping decrement.

Recent experiments in gas-filled hohlraums conducted on the Nova laser at Lawrence Livermore National Laboratory (LLNL) show that the laser spot on the hohlraum wall is effectively 150 μm closer to the laser entrance hole (LEH) than in empty hohlraum experiments.[3] We show that this spot motion can be interpreted as beam deflection occurring near the LEH by simulating these experiments using F3D,[8] a fully nonlinear, 3D fluid hydrodynamics code with paraxial light-wave propagation. A necessary component in effectively modeling the experiment is utilizing as input to F3D the beam structure of the unsmoothed Nova laser beams[6] as well as realistic plasma profiles generated by LASNEX. Our modeling shows that an unsmoothed Nova beam undergoes beam deflection at the LEH, which results in an effective shift in the beam centroid toward the LEH. When the beam is spatially smoothed by applying random phase plates (RPPs),[8,9] the centroid shift is reduced to within laser pointing accuracy. These results, which simulate the actual beam profiles at the wall, are in qualitative agreement with experiments, where the x-ray emission pattern was measured.

The second physical mechanism we address in this article is the effect of beam structure on channel formation by ultraintense laser light, a situation directly applicable to the hole-boring beam in the fast ignitor concept.[10] We have modified F3D to include relativistic corrections and the effect of charge separation.[11] In 3D simulations of a Gaussian beam with peak intensity 5.7×10^{17} W/cm^2 and a waist of 15 μm, or of an f/3 beam with the same amount of input power as the

Gaussian, the beam creates a channel through 1 mm of plasma with initially uniform density $n = 0.1n_c$ for the Gaussian beam or through 0.4 mm for the f/3 beam in a time $t = 15$ ps. However, when random phase aberrations are superposed on an f/3 laser beam, so that asymptotically the beam is f/3 but at best focus it is no longer diffraction limited (its spot size is 15 μm), a channel does not form through 400 μm of plasma at density $n = 0.1n_c$ in a time $t = 30$ ps.

After this introduction, the second section of this article addresses beam deflection in two subsections: first we present our analysis, then the results of our modeling. The third section is devoted to channel formation of ultraintense laser light. In the fourth section, we conclude with a discussion of our results.

Laser-Beam Deflection by Transverse Plasma Flow

Beam deflection has been a topic of vigorous interest in the past few years because of its potential to degrade the implosion symmetry of targets in gas-filled hohlraums. In 1982, Short, Bingham, and Williams[12] analyzed the plasma dispersion relation with transverse flow, and showed that the spatial growth rate was enhanced and peaked at values of M less than about unity. A series of Nova gas-filled hohlraum experiments inspired H. A. Rose[13] to suggest that transverse plasma flow could explain the observed deflection of backscattered light. Hinkel, Williams, and Still[14] simulated beam deflection for laser beams with spatial (RPP) and temporal (SSD[15]) beam smoothing. They showed that RPP beams deflect both supersonically (by forward Brillouin scatter between different k-components of the RPP beam) and subsonically as well, and that SSD mitigates the deflection. In this present work, we extend our previous work by simulating unsmoothed beams, and by deriving an analytic expression that is valid for circular and elliptic Gaussian beams for all values of the transverse flow Mach number M. Our present work, in the appropriate limits, is in agreement with that of Ghosal and Rose,[7] who performed a linear analysis of beam deflection. In addition to the gas-filled hohlraum experiments on Nova, there have been exploding foil experiments performed on Nova[4] and on the Janus laser[5] at LLNL that show an intensity-dependent beam deflection.

The equations of motion governing the coupling of the laser light to the density perturbation[1] in the paraxial approximation are

$$\left(2ik_0\partial_z + \nabla_\perp^2\right)\psi = \left(\omega_{\mathrm{pe}}^2 / c^2\right)\delta\bar{n}\psi \tag{1a}$$

and

$$\left[\left(\partial_t + u\partial_x + \nu\right)\left(\partial_t + u\partial_x\right) - C_s^2\nabla_\perp^2\right]\delta\bar{n} = \frac{1}{4}C_s^2\left(v_0/v_e\right)^2\nabla_\perp^2|\psi|^2 \quad . \tag{1b}$$

Here, ψ is the light-wave vector potential scaled to its peak value, $\delta\bar{n}$ is the fractional density perturbation, k_0 is the laser wave number, ω_{pe} is the electron-plasma frequency, c is the speed of light, ν is the ion damping rate, u is the transverse plasma flow, C_s is the sound speed, v_0 is the electron quiver velocity in the peak light wave electric field, and v_e is the electron thermal velocity. An additional approximation, consistent with the paraxial approximation, is that density perturbations are transverse to the forward-propagating light wave.

Beam Deflection: Analysis

A simple 1D argument demonstrates that the plasma density response is downstream from the light wave when transverse flow is present. Assume that the light wave is legislated, i.e., that ψ is known and given. Then, in steady state, a 1D version of Eq. 1 takes the form

$$\left[\left(u\partial_x + \nu\right)u\partial_x - C_s^2\partial_x^2\right]\delta\bar{n} = \frac{1}{4}C_s^2\left(v_0/v_e\right)^2\partial_x^2|\psi|^2 \quad . \tag{2}$$

Eq. 2 can be integrated once (for constant u), giving

$$\left[\partial_x - \frac{u\nu}{C_s^2 - u^2}\right]\delta\bar{n} = -\frac{1}{4}\frac{C_s^2\left(v_0/v_e\right)^2\partial_x^2|\psi|^2}{C_s^2 - u^2} \quad . \tag{3}$$

A local density minimum means that $\partial_x(\delta\bar{n}) = 0$, and thus

$$\delta\bar{n}\big|_{\partial_x(\delta\bar{n})=0} = \frac{1}{4}\frac{C_s^2}{u\nu}\left(\frac{v_0}{v_e}\right)^2\partial_x|\psi|^2 \quad . \tag{4}$$

In the absence of damping, the minimum of the density profile coincides with the maximum of the ponderomotive potential. Where the density has a local minimum and where $\nu > 0$ and $u > 0$, we have $\partial_x|\psi|^2 < 0$. Thus, the density well does not line up with the peak in the ponderomotive potential; rather, it is displaced downstream from the potential maximum where $\partial_x|\psi|^2 < 0$.

It now remains to show that the light wave is refracted into the displaced density well, thereby moving downstream as well. We obtain equations for the beam centroid and the beam width by taking intensity-weighted moments of Eq. 1a,

$$\frac{\partial^2}{\partial z^2}\left\langle \mathbf{x}_\perp \right\rangle = \frac{\partial}{\partial z}\left\langle \tilde{\mathbf{k}}_\perp \right\rangle = -\frac{\omega_{\mathrm{pe}}^2}{2\left(k_0 c\right)^2}\left\langle \nabla_\perp \delta\overline{n} \right\rangle \ , \tag{5a}$$

and

$$\frac{\partial^2}{\partial z^2}\left\langle \left(\mathbf{x}_\perp - \left\langle \mathbf{x}_\perp \right\rangle\right)^2 \right\rangle =$$

$$\times 2\left\{ \left\langle \left(\tilde{\mathbf{k}}_\perp - \left\langle \tilde{\mathbf{k}}_\perp \right\rangle\right)^2 \right\rangle - \frac{\omega_{\mathrm{pe}}^2}{\left(k_0 c\right)^2}\left\langle \left(\mathbf{x}_\perp - \left\langle \mathbf{x}_\perp \right\rangle\right)\cdot\left(\nabla_\perp \delta\overline{n}\right) \right\rangle \right\} \tag{5b}$$

where $\left\langle \mathbf{x}_\perp \right\rangle \equiv \int d^2 x_\perp \psi^* \mathbf{x}_\perp \psi$,

$\left\langle \tilde{\mathbf{k}}_\perp \right\rangle \equiv \left\langle \mathbf{k}_\perp / \mathbf{k_0} \right\rangle = -\left(i/k_0\right)\int d^2 x_\perp \psi^* \nabla_\perp \psi$, etc.

Eq. 5a describes the beam centroid motion as a function of propagation distance. The transverse density gradient refracts the light to regions of lower electron density. Eq. 5b governs the beam width as a function of propagation distance. As the beam propagates through plasma, the beam width will increase if diffraction (first term on right-hand side of Eq. 5b) dominates self-focusing (second term on right-hand side of Eq. 5b), and it will decrease if self-focusing dominates diffraction.[16]

We envisage three regimes for beam deflection. Well below the critical power for self-focusing, where the beam width is not modified by ponderomotive effects, Eq. 5a can be integrated in the *z* direction using the unperturbed beam width. In this limit, test calculations using our code F3D show agreement with our analytic results. Approaching critical power, a self-consistent solution of Eqs. 5a and 5b is required to determine the beam deflection rate. Above critical power, a self-consistent solution for the beam width will determine the deflection rate up to the point where beam breakup occurs, beyond which a single-beam model no longer applies.

It is beyond the scope of this present work to self-consistently evolve the beam width. Therefore we shall legislate a beam width and focus our attention on solving Eq. 5a.

We outline the methodology for solving Eq. 5a by first solving for $\langle \delta\overline{n} \rangle$, where, again, the brackets denote an intensity-weighted average. By Fourier transforming Eq. 1b and solving for $\delta\overline{n}\left(\mathbf{k}_\perp\right)$, we find that[14]

$$\langle \delta\overline{n} \rangle = -\frac{1}{16\pi^2}\left(\frac{v_0}{v_{\mathrm{e}}}\right)^2 \int \frac{d^2 k_\perp k_\perp^2 \, g\left(\mathbf{k}_\perp\right) g\left(-\mathbf{k}_\perp\right) / g(0)}{\left(1 - M^2\right)k_x^2 + k_y^2 + i\overline{\nu} M k_\perp k_x} \ , \tag{6}$$

where $M \equiv u / C_{\mathrm{s}}$ is the transverse Mach number (here we have assumed that the flow is in the *x* direction), $\overline{\nu} \equiv \nu / \left(k_\perp C_s\right)$ is the ion damping decrement, and $g(\mathbf{w})$ is the Fourier transform of $|\psi|^2$ evaluated at $\mathbf{k} = \mathbf{w}$. Similarly, when the Fourier transform of Eq. 1b is substituted into Eq. 5a, we obtain

$$\frac{\partial}{\partial z}\left\langle \tilde{\mathbf{k}}_\perp \right\rangle = \frac{i\omega_{\mathrm{pe}}^2}{32\pi^2\left(k_0 c\right)^2}\left(\frac{v_0}{v_{\mathrm{e}}}\right)^2$$

$$\times \int \frac{d^2 k_\perp \mathbf{k}_\perp k_\perp^2 \, g\left(\mathbf{k}_\perp\right) g\left(-\mathbf{k}_\perp\right) / g(0)}{\left(1 - M^2\right)k_x^2 + k_y^2 + i\overline{\nu} M k_\perp k_x} \ . \tag{7}$$

Eqs. 6 and 7 can be integrated over angle for any wave field *g* that can be expanded in a Fourier–Bessel series. However, for definiteness, we assume

$$g\left(\mathbf{k}_\perp\right) = \pi\sigma_x\sigma_y \exp\left[-k_x^2\sigma_x^2/4 - k_y^2\sigma_y^2/4\right]$$

and

$$\psi\left(\mathbf{x}_\perp\right) = \exp\left[-x^2/\left(2\sigma_x^2\right) - y^2/\left(2\sigma_y^2\right)\right] \ ,$$

i.e., the beam field is a Gaussian in real space with beam width σ_x in the *x*-direction and σ_y in the *y*-direction.

It is then easy to perform the radial portion of the integrands of Eqs. 6 and 7, yielding

$$\langle \delta\overline{n} \rangle = -\frac{1}{8}\left(\frac{v_0}{v_{\mathrm{e}}}\right)^2 \left\{ 1 + \frac{M^2}{2\pi}\frac{\sigma_y^2}{\sigma_x^2}\int_0^{2\pi} \frac{d\theta \cos^2\theta\left[\tilde{\alpha}^2 - 1 - M^2\overline{\nu}^2\left(\sigma_x^2/\sigma_y^2\right)/2 - \varepsilon^2\overline{\nu}^2\cos^2\theta\right]}{\left[1 - \left(1 - \tilde{\alpha}^2\right)\cos^2\theta\right]^2 + \tilde{\beta}^2\cos^4\theta} \right\} \tag{8}$$

and

$$\frac{\partial}{\partial z}\left\langle \tilde{k}_x \right\rangle = \frac{\sqrt{2}}{64\sqrt{\pi}}\left(\frac{v_0}{v_{\mathrm{e}}}\right)^2 \frac{n}{n_{\mathrm{c}}}\left(\frac{\omega_0}{k_0 c}\right)^2 \frac{M\overline{\nu}\sigma_y}{\sigma_x^2}\int_0^{2\pi} \frac{d\theta\left[1 + \varepsilon^2\cos^2\theta\right]^{3/2}}{\left[1 - \left(1 - \tilde{\alpha}^2\right)\cos^2\theta\right]^2 + \tilde{\beta}^2\cos^4\theta} \ , \tag{9}$$

where $\tilde{\alpha}^2 \equiv \left(\sigma_y^2/\sigma_x^2\right)\left[1 - M^2\left(1 - \bar{\nu}^2/2\right)\right]$ and $\tilde{\beta} \equiv \left(\sigma_y^2/\sigma_x^2\right)M^2\bar{\nu}$. The above expressions are valid through order $\bar{\nu}^2$, i.e., corrections of order $(M^2\bar{\nu}^4)$ have been dropped. The beam eccentricity is measured by $\varepsilon^2 \equiv \sigma_y^2/\sigma_x^2 - 1$. Note that in the above expression, the component of $\tilde{\mathbf{k}}_\perp$ that is nonzero is that in the flow direction, i.e., $\tilde{k}_x$.

If we use the identity $\cos^2\theta = \left[1 + \cos(2\theta)\right]/2$, make the change of variable $\phi = 2\theta$, and integrate about the unit circle by setting $z = \exp(i\phi)$, the expression for $\langle\delta\bar{n}\rangle$ can be determined by summing over the residues inside the unit circle,

$$\langle\delta\bar{n}\rangle = -\frac{1}{8}\left(\frac{v_0}{v_\mathrm{e}}\right)^2 \left\{1 + \frac{\frac{M^2}{\sqrt{2}}\frac{\sigma_y^2}{\sigma_x^2}}{\left[\left(1-\tilde{\alpha}^2\right)^2 + \tilde{\beta}^2\right]} \left\{\begin{array}{l} \left[\frac{\sigma_y^2}{\sigma_x^2}\left(1 - M^2\right) - 1 + \varepsilon^2\bar{\nu}^2\right]\left\{\sqrt{2} - \frac{\sqrt{\sqrt{\tilde{\alpha}^4 + \tilde{\beta}^2} + \tilde{\alpha}^2}}{\sqrt{\tilde{\alpha}^4 + \tilde{\beta}^2}}\right\} \\ + \left[\left(\tilde{\alpha}^2 - 1\right)\left(\frac{M^2\bar{\nu}^2\sigma_y^2}{2\sigma_x^2} - \varepsilon^2\bar{\nu}^2\right) + \tilde{\beta}^2\right]\frac{\sqrt{\sqrt{\tilde{\alpha}^4 + \tilde{\beta}^2} - \tilde{\alpha}^2}}{\tilde{\beta}\sqrt{\tilde{\alpha}^4 + \tilde{\beta}^2}} \end{array}\right\}\right\} . \tag{10}$$

To determine the beam deflection rate, we perform the integration in Eq. 9 by expanding for small ellipticity, i.e., $|\varepsilon|^2 << 1$. Then, along the unit circle, the second term in the square brackets of the numerator of Eq. 9 is small compared to the first, or $\left[1 + \varepsilon^2\cos^2\theta\right]^{3/2} \cong 1 + (3/2)\varepsilon^2\cos^2\theta$. Summing over the residues, we then obtain

$$\frac{\partial}{\partial z}\left\langle\tilde{k}_x\right\rangle = \frac{\sqrt{\pi}}{32}\left(\frac{v_0}{v_\mathrm{e}}\right)^2 \frac{n}{n_\mathrm{c}}\left(\frac{\omega_0}{k_0 c}\right)^2 \frac{M\bar{\nu}}{\sigma_x}\frac{\sigma_y}{\sigma_x} \left\{\begin{array}{l} \frac{\sqrt{\sqrt{\tilde{\alpha}^4 + \tilde{\beta}^2} - \tilde{\alpha}^2}}{\tilde{\beta}\sqrt{\tilde{\alpha}^4 + \tilde{\beta}^2}} \\ + \frac{(3/2)\varepsilon^2}{\left(1 - \tilde{\alpha}^2\right)^2 + \tilde{\beta}^2}\left[\begin{array}{c} \sqrt{2} - \frac{\sqrt{\sqrt{\tilde{\alpha}^4 + \tilde{\beta}^2} + \tilde{\alpha}^2}}{\sqrt{\tilde{\alpha}^4 + \tilde{\beta}^2}} \\ -\left(\tilde{\alpha}^2 - 1\right)\frac{\sqrt{\sqrt{\tilde{\alpha}^4 + \tilde{\beta}^2} - \tilde{\alpha}^2}}{\tilde{\beta}\sqrt{\tilde{\alpha}^4 + \tilde{\beta}^2}} \end{array}\right] \end{array}\right\} . \tag{11}$$

Figure 1 depicts $\langle\delta\bar{n}\rangle$ vs Mach number for both a circular beam (black curve), where $\sigma_y = \sigma_x$, and for an elliptic beam (gray curve), where $\sigma_y = 2\sigma_x$. In both cases, the density response near $M = 1$ is almost triple the response at $M = 0$. This demonstrates that the process of filamentation[14] is enhanced by near-sonic transverse flow.

The density response of the elliptic beam is slightly greater than that of the circular beam for $\varepsilon^2 > 0$ around the sonic surface. As σ_y becomes large compared to σ_x, we recover the 2D limit, where, for $M > 1$, the density response is positive, i.e., there is a density enhancement rather than a density cavity.

In the subsonic regime, for a circular beam, where $1 - M^2 >> M\bar{\nu}$, $M < 1$, and $\varepsilon = 0$, the expression for $\langle\delta\bar{n}\rangle$ as given by Eq. 10 reduces to

$$\langle\delta\bar{n}\rangle_{\mathrm{subsonic},\sigma_x = \sigma_y} \sim -\frac{1}{8}\left(\frac{v_0}{v_\mathrm{e}}\right)^2 \frac{1}{\sqrt{1 - M^2}} . \tag{12}$$

For near-sonic flow, we evaluate Eq. 10 with $M = 1$ for a circular beam to find

$$\langle\delta\bar{n}\rangle_{\text{near-sonic},\sigma_x = \sigma_y} \sim -\frac{1}{8}\left(\frac{v_0}{v_\mathrm{e}}\right)^2 \frac{1}{2\bar{\nu}^{1/2}} , \tag{13}$$

i.e., the density response for near-sonic flow is a resonant response that is limited by the damping, or, in the limit of weak damping, would be limited by nonlinear effects.[17] For supersonic transverse flow, where $M^2 - 1 >> M\bar{\nu}$, we find that Eq. 10 reduces to

$$\langle\delta\bar{n}\rangle_{\mathrm{supersonic},\sigma_x = \sigma_y} \sim -\frac{\bar{\nu}}{16}\left(\frac{v_0}{v_\mathrm{e}}\right)^2 \frac{2M^2 - 1}{\left(M^2 - 1\right)^{3/2}} . \tag{14}$$

The density response of an elliptic beam is qualitatively different from that of a circular beam in the supersonic regime. When the beam is circular, the

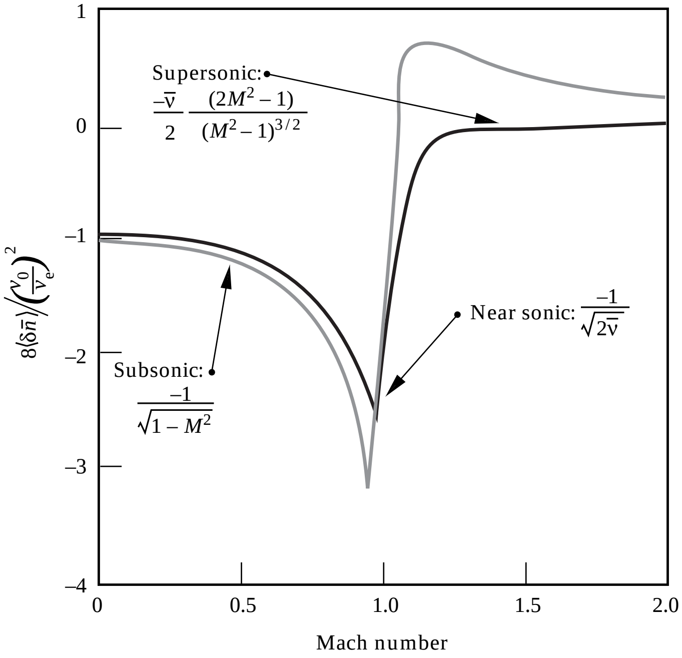

FIGURE 1. The average fractional density perturbation $\langle\delta\bar{n}\rangle$, normalized to $(v_0/v_e)^2/8$, vs Mach number when the ion damping decrement $\bar{\nu} = 0.1$. The black curve is for a circular beam, and the gray curve is for an elliptic beam, where $\sigma_y/\sigma_x = 2$. The average value of $\langle\delta\bar{n}\rangle$ is 2.5 times greater for the circular beam in near-sonic transverse flow than in the absence of transverse flow. (50-00-0898-1704pb01)

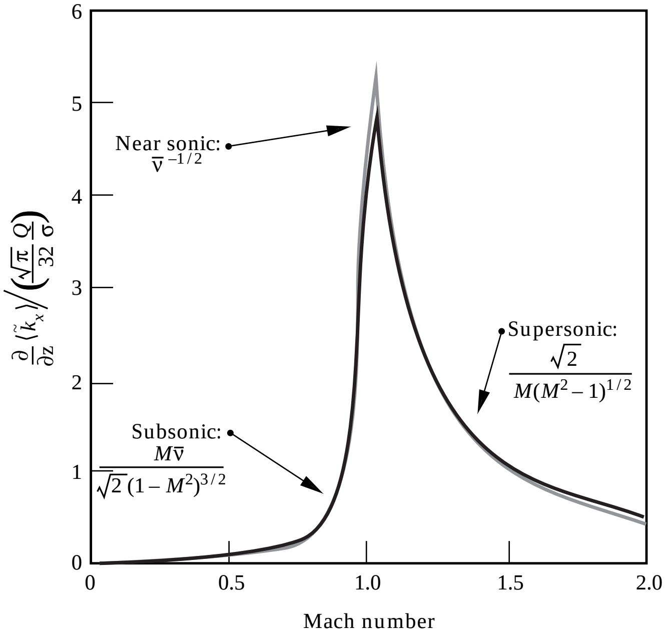

FIGURE 2. Beam deflection rate vs Mach number when the ion damping decrement $\bar{\nu} = 0.1$. The black curve is for a circular beam, and the gray curve is for a slightly elliptic beam, where $\sigma_y^2/\sigma_x^2 = 1.1$. The primary contribution to the beam deflection rate occurs when the transverse flow is nearly sonic. (50-00-0898-1705pb01)

density response is always negative. However, when the beam is elliptic, such that $\sigma_y > \sigma_x$, i.e., the beam is narrower in the flow direction, the density response changes sign, becoming positive as it is in the $\sigma_x = 0$ limit of a line-focused beam.

In Figure 2, we plot the beam deflection rate vs Mach number for a circular beam (black curve) and an elliptic beam (gray curve). (In the circular beam limit, where $\sigma_y = \sigma_x \equiv \sigma$, only the first term in the large curly bracket of Eq. 11 survives.) The largest beam deflection rate occurs for near-sonic transverse flow. In the subsonic regime,

$$\frac{\partial}{\partial z}\left\langle \tilde{k}_x \right\rangle_{\text{subsonic},\sigma_x = \sigma_y}$$

$$\sim \frac{1}{32}\sqrt{\frac{\pi}{2}}\left(\frac{v_0}{v_e}\right)^2\left(\frac{n}{n_c}\right)\left(\frac{\omega_0}{k_0c}\right)^2\frac{1}{\sigma}\frac{M\bar{\nu}}{\left(1-M^2\right)^{3/2}} . \quad (15)$$

Subsonically, the deflection rate scales linearly with the damping decrement and with Mach number, and increases as $M \to 1$.

In the near-sonic regime, for a circular beam, Eq. 11 reduces to

$$\frac{\partial}{\partial z}\left\langle \tilde{k}_x \right\rangle_{\text{near-sonic},\sigma_x = \sigma_y}$$

$$\sim \frac{\sqrt{\pi}}{32}\left(\frac{v_0}{v_e}\right)^2\left(\frac{n}{n_c}\right)\left(\frac{\omega_0}{k_0c}\right)^2\frac{1}{\sigma\bar{\nu}^{1/2}} . \quad (16)$$

As with the density response, the beam deflection rate exhibits resonant behavior near $M = 1$, which is limited by the inclusion of damping.

This expression can be integrated once when the density profile is constant, yielding

$$\left\langle \tilde{k}_x \right\rangle \sim \frac{\sqrt{\pi}}{32}\left(\frac{v_0}{v_e}\right)^2\left(\frac{n}{n_c}\right)\left(\frac{\omega_0}{k_0c}\right)^2\frac{1}{\bar{\nu}^{1/2}}\frac{L}{\sigma} , \quad (17)$$

where $\left\langle \tilde{k}_x \right\rangle$ is the deflection angle in radians. If the hot spot length L_s, which for a Gaussian beam is the Rayleigh length, is long compared to the transverse-flow scale length L_u, then in the above equation, $L = L_u$, i.e., the transverse-flow scale length is the limiting length in the problem. If L_s is short compared to L_u, then L_s is the length in question. For an RPP beam, $\sigma \sim f\lambda_0$ and $L_s \sim 8f^2\lambda_0$, where f is the f-number of the optic, so

$$\left\langle k_x \right\rangle \sim \frac{\sqrt{\pi}}{32}\left(\frac{v_0}{v_e}\right)^2\left(\frac{n}{n_c}\right)\left(\frac{\omega_0}{k_0 c}\right)^2 \frac{1}{\bar{\nu}^{1/2}}\frac{L_u}{f\lambda_0},\ L_u << L_s\,; \quad (18a)$$

and

$$\left\langle k_x \right\rangle \sim \frac{\sqrt{\pi}}{4}\left(\frac{v_0}{v_e}\right)^2\left(\frac{n}{n_c}\right)\left(\frac{\omega_0}{k_0 c}\right)^2 \frac{f}{\bar{\nu}^{1/2}}\ ,\quad L_s << L_u\,. \quad (18b)$$

This scaling does not account for multispeckle phenomena in an RPP beam, where light leaving one density depression can enter another density depression and continue to get swept downstream over a length longer than L_s.

Finally, in the supersonic regime, Eq. 11 takes the form

$$\frac{\partial}{\partial z}\left\langle \tilde{k}_x \right\rangle_{\text{supersonic},\sigma_x = \sigma_y}$$

$$\sim \frac{\sqrt{2\pi}}{32}\left(\frac{v_0}{v_e}\right)^2\left(\frac{n}{n_c}\right)\left(\frac{\omega_0}{k_0 c}\right)^2 \frac{1}{\sigma M}\frac{1}{\left(M^2-1\right.} \quad (19)$$

For $M >> 1$, the beam deflection rate scales as $1/M^2$, and is independent of the damping decrement. In all three regimes, the beam deflection rate scales with the figure of merit $Q \equiv \left(v_0/v_e\right)^2\left(n/n_c\right)\left(\omega_0/k_0 c\right)^2$. In these limiting regions, our beam deflection rate results are in agreement with those of Ghosal and Rose.[7]

For a single Gaussian hotspot with circular cross section focused at $z = z_0$, Eq. 11 reduces to

$$\frac{\partial}{\partial z}\left\langle \tilde{k}_x \right\rangle_{\text{circular}} = \frac{\sqrt{\pi}}{32}\left(\frac{v_0}{v_e}\right)^2\left(\frac{n}{n_c}\right)\left(\frac{\omega_0}{k_0 c}\right)^2$$

$$\times \frac{M\bar{\nu}}{\sigma_0}\frac{1}{\left[1+\left(z-z_0\right)^2\Big/\left(k_0^2\sigma_0^4\right)\right]^{3/2}}\frac{\sqrt{\sqrt{\tilde{\alpha}^4+\tilde{\beta}^2}-\tilde{\alpha}^2}}{\tilde{\beta}\sqrt{\tilde{\alpha}^4+\tilde{\beta}^2}}\ . \quad (20)$$

Here, v_0 and σ_0 are evaluated at the focus, $z = z_0$.

For constant density and flow, this expression can be integrated to give the total deflection of the Gaussian beam:

$$\left\langle \tilde{k}_x \right\rangle = \frac{\sqrt{\pi}}{16}\left(\frac{v_0}{v_e}\right)^2 \frac{n/n_c}{1-n/n_c}k_0\sigma_0$$

$$\times \frac{M\bar{\nu}}{\tilde{\beta}}\frac{\sqrt{\sqrt{\tilde{\alpha}^4+\tilde{\beta}^2}-\tilde{\alpha}^2}}{\sqrt{\tilde{\alpha}^4+\tilde{\beta}^2}}\ . \quad (21)$$

The above results, depicted in Figures 1 and 2, indicate that we should concentrate our simulation efforts near the $M = 1$ surface, where both $\langle\delta\bar{n}\rangle$ and the deflection rate peak.

In the weak damping limit, where a steady state is not reached, one would expect subsonic deflection from transient effects and self-induced bandwidth rather than from damping, and near $M = 1$, nonlinear effects[17] would dominate the physics. In the experiments modeled in the next section, the plasma is composed of CH, with a damping decrement $\bar{\nu} \cong 0.1$. In this regime we anticipate subsonic and supersonic deflection with the $M = 1$ resonance limited by damping.

Beam Deflection: Modeling Results

As mentioned earlier in this article, gas-filled hohlraum experiments on the Nova laser[3] show an effective spot motion of 150 μm toward the LEH that is reduced to 35 μm when RPPs are used on the laser beams. Near peak laser power, the plasma density and transverse flow profiles calculated by LASNEX[2] are depicted in Figure 3. The transverse flow profile is sheared, and is near sonic with a scale length of about 600 μm at the LEH. The plasma density is modeled as $n_e / n_c = .06 + .04\tanh\left(z / \lambda_0\right)$, where $\lambda_0 = 0.351$ μm. Here, z is chosen such that $n_e/n_c = .01$, where $M = 1$. The corresponding electron temperature is $T_e \approx 3$ keV.

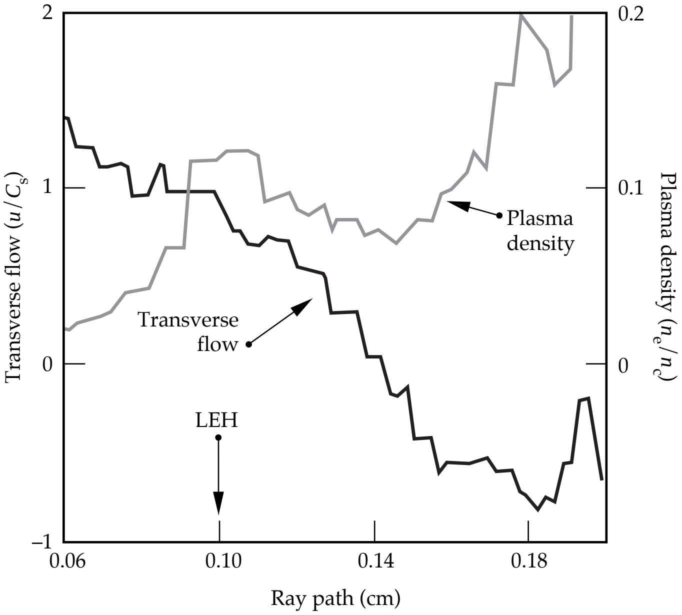

FIGURE 3. The transverse flow and plasma density profiles along a typical ray path in a methane-filled hohlraum near peak power on the Nova laser as calculated by LASNEX. The corresponding electron temperature is $T_e \approx 3$ keV, and the laser light wavelength is $\lambda_0 = 0.351$ μm. (50-00-0898-1706pb01)

It remains to specify the beam structure. The simulated unsmoothed Nova beam[6] 1 mm beyond best focus, which is the unsmoothed beam plane at the LEH, is markedly different in structure from the simulated RPP Nova beam[6,8,9] at best focus, which is its beam plane at the LEH. Both beams are f/4 and have similar average peak intensities. The speckle statistics of the beams are the same, but the unsmoothed Nova beam contains large coherent pieces, as well as large voids, which give rise to sub-spot-scale intensity modulations upon which the speckle statistics are superposed.

The F3D code models the speckle statistics of a beam about a given average intensity. Computational limitations inhibit modeling of the entire beam in one simulation (250 μm × 250 μm × 1000 μm). Thus, we have taken the unsmoothed and RPP beams, and averaged the intensities in the initial beam cross section on a 28 μm × 28 μm spatial scale. Each 28 μm × 28 μm piece of the beam then has an average intensity at which a simulation is performed.

These spatially smoothed average intensities are plotted in Figure 4. The peak value for the RPP beam is 3×10^{15} W/cm^2, as opposed to 1×10^{16} W/cm^2 for the unsmoothed beam. An F3D simulation was performed at each spatially smoothed average intensity in the beam over a propagation distance of 350 μm. At $z = 350$ μm, each piece of the beam is placed back in its original beam position, and the entire beam is paraxially propagated through 1 mm of plasma at density $n = 0.1n_c$, roughly the distance from the LEH to the wall. The intensity distribution vs wall position of the RPP and unsmoothed beams is plotted in Figure 5. The peak of the RPP beam is located within 50 μm of where it was pointed, whereas the centroid of the unsmoothed beam is ~100 μm closer to the LEH than it was pointed, in agreement with experimental results. Moreover, the general structure of the predicted laser intensity on the wall, of a wide "plateau" or "shoulder" in the flow direction, is in agreement with the x-ray emission profile measurements. Thus we see that it is the difference in the intensity distributions of the beams, i.e., the beam structure, that accounts for the change in effective wall position for unsmoothed vs RPP beams.

A secondary feature that also enhances the deflection of the unsmoothed beam arises from the focusing geometry. The unsmoothed f/4 Nova beam is focused 1 mm outside the LEH, and in the beam plane at the LEH, the hot spots in the beam are more accurately described by f/6 speckle statistics. Because an f/6 speckle is longer [by a factor of $(3/2)^2$] and wider [by a factor of (3/2)] than an f/4 speckle, the spatial region of a given hot spot over which beam deflection can occur is larger, thus yielding more beam deflection.

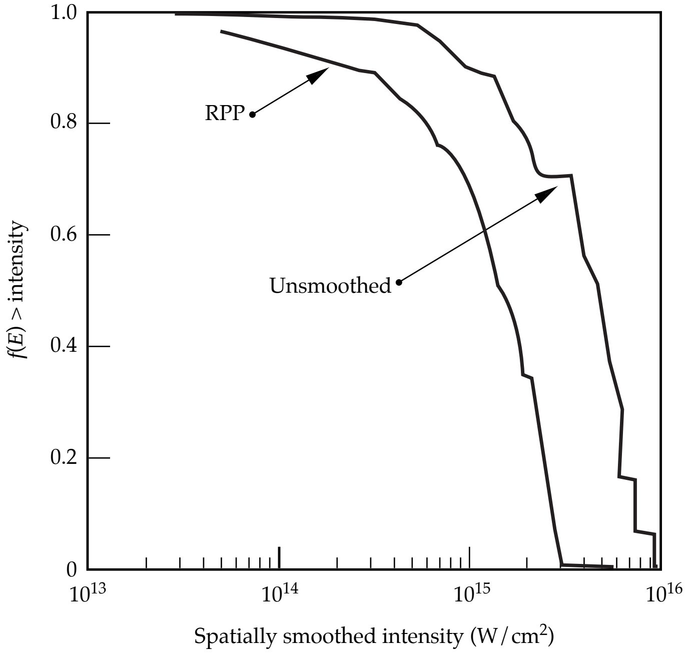

FIGURE 4. The running sum of the intensity distributions of RPP and unsmoothed Nova beams vs intensity when the intensity is spatially averaged on a 28 μm × 28 μm scale. The RPP beam has a peak spatially averaged intensity of 3×10^{15} W/cm^2, whereas the unsmoothed beam peaks at 1×10^{16} W/cm^2. (50-00-0898-1707pb01)

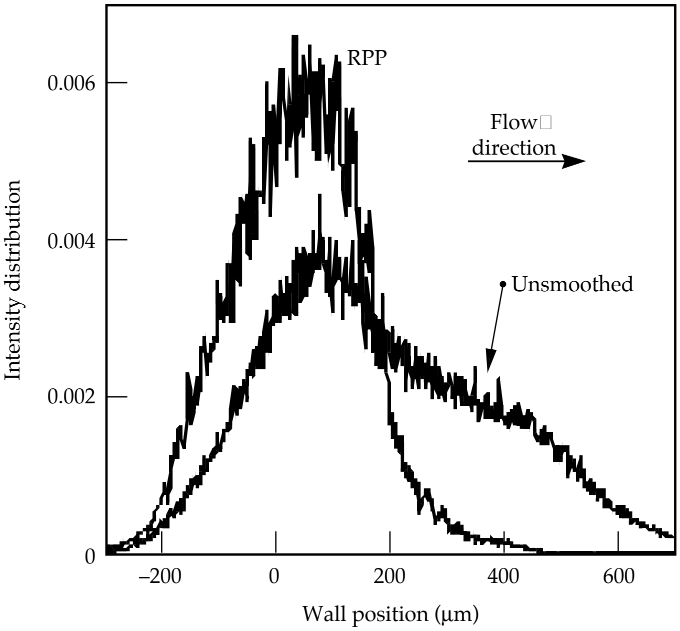

FIGURE 5. The intensity distribution vs wall position of the RPP and unsmoothed Nova beams near peak power. The peak of the RPP beam is located within 50 μm of where it was pointed, whereas that of the unsmoothed beam is 100 μm closer to the LEH than pointed. The unsmoothed beam also has a high shoulder off the peak in the flow direction. (50-00-0898-1708pb01)

Channel Formation by Ultraintense Laser Light

Channeling of intense laser light is crucial to the fast ignitor concept,[10] where light must reach the overdense regime. Prior to channeling the intense laser light, a channel must be *created* by the "hole-boring" pulse. We have begun to examine and analyze beam propagation in underdense plasma in an effort to better understand the channel formation process.

We utilize a relativistic form of F3D[11] to study channeling. In this form, the index of refraction in the light-wave equation has been modified according to the replacement $n_e \to n_e / \gamma$, where $\gamma \equiv (1 + u_0^2 / c^2)^{1/2}$, with $u_0 \equiv eA_0 / (m_e c)$. [Here, A_0 is the RMS value of the vector potential of the light wave.] This accounts for relativistic corrections to the electron mass. We have modified the ponderomotive drive in the momentum equation by making the replacement $\nabla u_0^2 / 2 \to c^2 \nabla\gamma$, so that momentum is conserved. At very high intensities, the ponderomotive drive then scales as $c\nabla u_0$ rather than as $\nabla u_0^2 / 2$ as it does at moderate intensities where $\gamma \approx 1$. Finally, we have implemented a charge-separation model similar to that of Sun et al.,[18] where $n_e = \max\left[0, Zn_i + \left(m_e c^2\right) / \left(4\pi e^2\right) \nabla_\perp^2 \gamma\right]$. Here, n_i is the ionic density, m_e is the electronic mass, Z is the ionic charge, and e is the electronic charge. This charge-separation model permits the electrons to be blown out of the channel by the ponderomotive force on very short (sub-picosecond) time scales, inducing a charge separation that then draws the ions out of the channel as well. On the time scale of the simulations presented below (30 ps), the charge-separation term has negligible effect, as the ions have had time to move.

This fluid model does not include such effects as Raman forward scatter (RFS), plasma heating, or thermal filamentation. RFS and plasma heating, which are included in PIC simulations,[19] would act to deplete the pump and create hot electrons in the channel, thereby limiting the ability to create a channel. Thus, these fluid simulations place an upper bound on the channel depth, and hence on the ability to create a channel.

We have propagated a 30-ps FWHM (full width at half maximum) Gaussian beam with peak intensity 5.7×10^{17} W/cm^2 and a waist of 15 μm at best focus through 1 mm of underdense plasma at density $n_e = 0.1n_c$ and electron temperature $T_e = 2$ keV. The beam filaments into several pieces, and the main (central) filament contains 65 to 70% of the intensity. The laser beam has self-focused by an order of magnitude in intensity, because of both relativistic and ponderomotive effects. The central filament plasma density is at about $n_e = 0.01n_c$, and a channel forms through the entire 1 mm of plasma. We find that this process occurs for a range of FWHM spot sizes from 3 to 15 μm.

Figure 6 depicts the $x = 0$ slice of the laser amplitude (Figure 6a) and the plasma density (Figure 6b) for an unaberrated, super-Gaussian f/3 laser beam. Clearly, a channel has formed through 400 μm of $n_e = 0.1n_c$ plasma after 15 ps. We have ascertained that channel formation occurs for a wide range of cone angles, from f/3 to f/10.

We have also simulated beams with both random phase aberrations and spherical aberrations. Figure 7 shows the $x = 0$ slice of the laser amplitude (Figure 7a) and the plasma density (Figure 7b) for an f/3 laser beam with random phase aberrations, which expand the spot size at best focus to 15 μm. In Figure 7a, we observe 3 hot spots near best focus, located at $z = 180$ μm, which have self-focused and thereby increased the intensity by a factor of 2. In

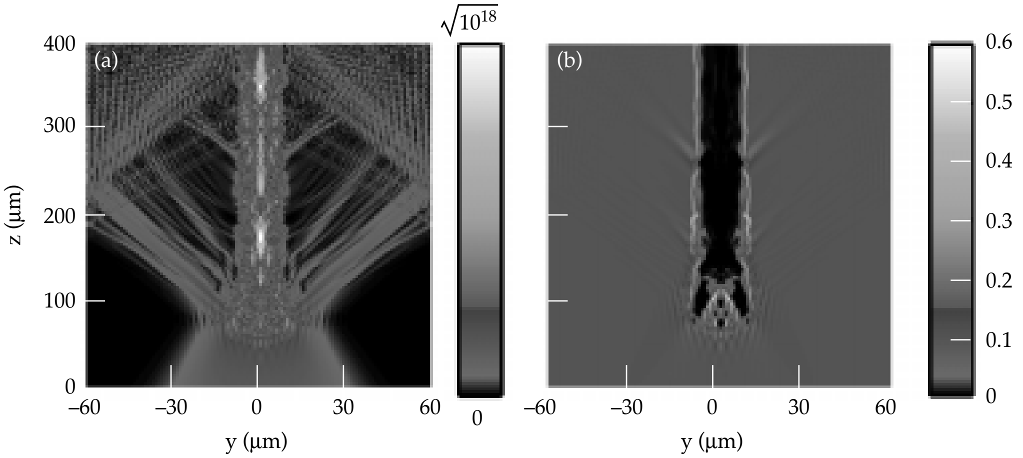

FIGURE 6. The laser amplitude and plasma density for an unaberrated, super-Gaussian f/3 beam with ~3 TW of input power. After 15 ps, the beam has created a channel through 400 μm of plasma at density $n_e = 0.1n_c$. (50-00-0898-1709pb01)

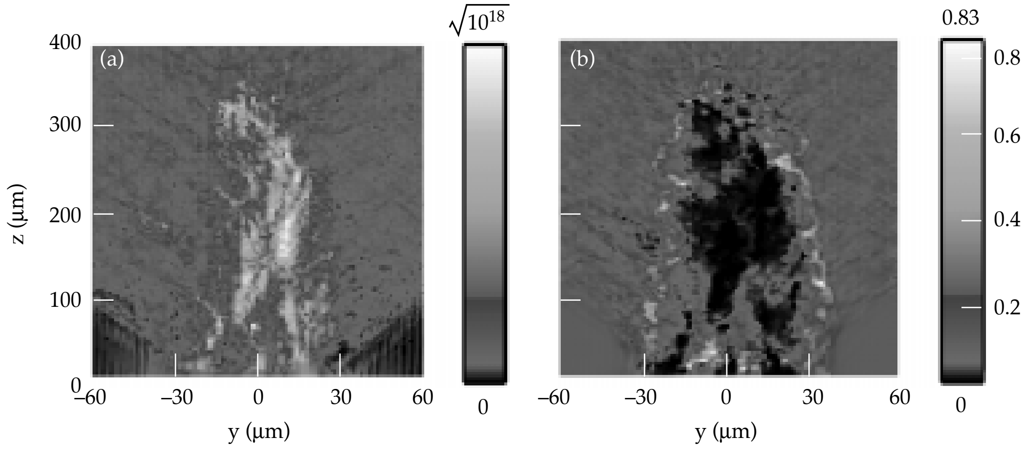

FIGURE 7. The laser amplitude and plasma density for a phase-aberrated f/3 beam with a spot size of 15 μm at best focus and with ~3 TW of input power. After 30 ps, the beam has failed to channel through 400 μm of plasma at density $n_e = 0.1n_c$, whereas a diffraction-limited f/3 beam creates an evacuated channel within 15 ps.
(50-00-0898-1710pb01)

Figure 7b, plasma has been pushed out of the regions where the beam is most intense. The beam structure, i.e., the presence of multiple hot spots, locally increases the intensity, but not globally. Thus relativistic and ponderomotive self-focusing is limited to the hot-spot regions, from which plasma density is expelled. With either random phase or spherical aberrations, a channel does not form through 400 μm of $n_e = 0.1n_c$ plasma in 30 ps, even though the beam contained the same amount of power (~3 TW) as the diffraction-limited beam. We thus conclude that aberrated beams do not channel as effectively as diffraction-limited beams.

Conclusions

In summary, we have shown that a predictive capability requires a model that contains the important beam-structure characteristics. We have presented two examples where the beam structure was essential.

In the first example, we studied beam deflection caused by transverse flow. We derived a global formula for the steady-state density response and beam deflection rate, valid for all Mach numbers. In the weak damping limit, when a steady state may not be reached, the effective damping decrement $\bar{\nu}$ can be estimated by the magnitude of the transient density response $\partial_t(\delta\bar{n})/\delta\bar{n}$. In practice, the $\bar{\nu} \to 0$ limit is never achieved because of residual time-dependent effects such as transients, self-induced bandwidth, and background evolution. Also, in the weak damping limit, nonlinear effects become important in the near-sonic regime. In the subsonic regime, the beam deflection rate scales linearly with the damping decrement and with Mach number, and scales inversely with $(1 - M^2)^{3/2}$. The density response is independent of the damping decrement in this regime, and scales inversely as $(1 - M^2)^{1/2}$. Around $M = 1$, damping limits the resonant response, and both the beam deflection rate and the density response scale as $\bar{\nu}^{-1/2}$. In the supersonic regime, the beam deflection rate is independent of the damping decrement, and scales as $1/[M(M^2 - 1)^{1/2}]$. Here, the density response is proportional to the damping decrement, and scales as $1/(M^2 - 1)^{3/2}$. Such analysis can be used to formulate a reduced description in models where laser propagation is not treated in detail.[2]

We have used this information to focus our modeling efforts where the transverse flow is near-sonic, which, in gas-filled hohlraums, is around the LEH. When the marked difference in the intensity distributions of the unsmoothed and RPP beams is folded into our modeling, we find that the intense portions of the unsmoothed beam deflect more (in agreement with our figure-of-merit scaling), thereby moving the wall spot centroid of the unsmoothed beam closer to the LEH than that of the RPP beam. Our results agree with the x-ray emission data in gas-filled hohlraum experiments.[3]

In our second example, we studied the effect of beam structure on channeling of intense laser beams. We determined that an idealized beam, containing only one hot spot with a peak intensity at 5.7×10^{17} W/cm^2, successfully creates a channel through underdense plasma at density $n = 0.1n_c$. However, if a more realistic beam model is used, such as one containing random phase aberrations but with the same input power as that of the idealized beam, we find that a channel does not form. Plasma density is expelled from the regions where the beam has hot spots, but builds up between the hot spots. This work has set in place the required framework to perform further analysis, such as determining the intensity threshold as a function of beam structure above which channel formation occurs.

Acknowledgments

We acknowledge valuable input from H. A. Rose, M. D. Rosen, R. L. Kauffman, S. G. Glendinning, L. J. Suter, B. F. Lasinski, K. G. Estabrook, and M. H. Key.

Notes and References

1. J. F. Drake et al., *Phys. Fluids* **17**, 778 (1974); D. W. Forslund, J. M. Kindel, and E. L. Lindman, ibid. **18**, 1002 (1975); *Advances in Plasma Physics*, edited by A. Simon and W. B. Thompson (Wiley, New York, 1976), Vol. 6.
2. G. Zimmerman and W. L. Kruer, *Comments Plasma Phys. Control. Fusion* **2**, 85 (1975).
3. L. V. Powers et al., *Advances in Laser Interaction with Matter and Inertial Fusion*, edited by J. M. Martinez-Val, E. Minguez, and J. M. Perlado (World Scientific, 1996); N. Delamater et al., *Phys. Plasmas* **3**, 2022 (1996).
4. J. D. Moody et al., *Phys. Rev. Lett.*, **77**, 1294 (1996).
5. P. E. Young et al., *Phys. Rev. Lett.* **81**, 1425 (1998).
6. S. N. Dixit et al., *Appl. Opt.* **32**, 2543 (1993); S. N. Dixit, M. D. Feit, M. D. Perry, and H. T. Powell, *Opt. Lett.* **21**, 1715 (1996).
7. S. Ghosal and H. A. Rose, *Phys. Plasmas* **4**, 2376 (1997).
8. R. L. Berger et al., *Phys. Fluids B* **5**, 2243 (1993).
9. Y. Kato and K. Mima, *Appl. Phys. B* **29**, 186 (1982).
10. M. Tabak et al., *Phys. Plasmas* **1**, 1626 (1994).
11. A. B. Langdon, D. E. Hinkel, B. F. Lasinski, and C. H. Still, *Bull. Am. Phys. Soc.* **42,** 1940 (1997).
12. R. W. Short, R. Bingham, and E. A. Williams, *Phys. Fluids* **25**, 2302 (1982).
13. H. A. Rose, Los Alamos National Laboratory, Los Alamos, NM, private communication, LLNL, 1995.
14. D. E. Hinkel, E. A. Williams, and C. H. Still, *Phys. Rev. Lett.* **77**, 1298 (1996).
15. S. Skupsky et al., *J. Appl. Phys.* **66,** 3456 (1989).
16. C. E. Max, *Phys. Fluids* **1**, 74 (1976); M. V. Goldman, K. Rypdal, and B. Hafizi, ibid. **23**, 945 (1980); J. J. Rasmussen and K. Rypdal, *Phys. Scr.* **3**, 481 (1986).
17. W. L. Kruer and J. H. Hammer, *Comments Plasma Phys. Control. Fusion* **18,** 85 (1997).
18. G.-Z. Sun, E. Ott, Y. C. Lee, and P. Guzdar, *Phys. Fluids* **30**, 526 (1987); M. D. Feit, J. C. Garrison, and A. M. Rubenchik, *Phys. Rev. E* **56**, 2394 (1997).
19. D. W. Forslund et al., *Phys. Rev. Lett.* 54, 558 (1985); W. B. Mori et al., ibid. **60**, 1298 (1988); K. C. Tzeng, W. B. Mori, and C. D. Decker, ibid. **76**, 3332 (1996).